Cancer Biology & Therapy 10:5, 438-447; September 1, 2010; © 2010 Landes Bioscience

Simultaneous optical coherence tomography and laser induced fluorescence imaging in rat model of ovarian carcinogenesis

Lida P. Hariri,[1] Erica R. Liebmann,[1] Samuel L. Marion,[2] Patricia B. Hoyer,[2] John R. Davis,[3] Molly A. Brewer[4] and Jennifer K. Barton[1,*]

[1]Department of Biomedical Engineering; [2]Department of Physiology; and [3]Department of Pathology; The University of Arizona; College of Medicine; Tucson, AZ USA; [4]Division of Gynecologic Oncology; Carol and Ray Neag Comprehensive Cancer Center; University of Connecticut; Farmington, CT USA

Key words: optical coherence tomography, fluorescence spectroscopy, optical imaging, ovarian cancer, post-menopausal rat model

Abbreviations: OCT, optical coherence tomography; LIF, laser induced fluorescence; VCD, 4-vinylcyclohexene diepoxide; DMBA, 7,12-dimethylbenz[a]anthracene; NADH, nicotinamide adenine dinucleotide; FAD, flavin adenine dinucleotide; H & E, hematoxylin and eosin; i.p., intraperitoneal; CL, corpus luteum; SCST, sex cord-stromal tumor

Determining if an ovarian mass is benign or malignant is an ongoing clinical challenge. The development of reliable animal models provides means to evaluate new diagnostic tools to more accurately determine if an ovary has benign or malignant features. Although sex cord-stromal tumors (SCST) account for 0.1–0.5% of ovarian malignancies, they have similar appearances to more aggressive epithelial cancers and can serve as a prototype for developing better diagnostic methods for ovarian cancer. Optical coherence tomography (OCT) and laser-induced fluorescence (LIF) spectroscopy are non-destructive optical imaging modalities. OCT provides architectural cross-sectional images at near histological resolutions and LIF provides biochemical information. We utilize combined OCT-LIF to image ovaries in post-menopausal ovarian carcinogenesis rat models, evaluating normal cyclic, acyclic and neoplastic ovaries. Eighty-three female Fisher rats were exposed to combinations of control sesame oil, 4-vinylcyclohexene diepoxide (VCD) to induce ovarian failure, and/or 7,12-dimethylbenz[a]anthracene (DMBA) to induce carcinogenesis. Three or five months post-treatment, 162 ovaries were harvested and imaged with OCT-LIF: 40 cyclic, 105 acyclic and 17 SCST. OCT identified various follicle stages, corpora lutea (CL), CL remnants, epithelial invaginations/inclusions and allowed for characterization of both cystic and solid SCST. Signal attenuation comparisons between CL and solid SCST revealed statistically significant increases in attenuation among CL. LIF characterized spectral differences in cyclic, acyclic and neoplastic ovaries attributed to collagen, NADH/FAD and hemoglobin absorption. We present combined OCT-LIF imaging in a rat ovarian carcinogenesis model, providing preliminary criteria for normal cyclic, acyclic and SCST ovaries which support the potential of OCT-LIF for ovarian imaging.

Introduction

Ovarian cancer is the fourth leading cause of cancer-related death among women in the US and the most deadly of all gynecologic malignancies, resulting in 15,520 deaths in 2008.[1] Sex cord-stromal tumors (SCST) of the ovary account for 0.1–0.5% of all ovarian malignancies and have a similar presentation to early stage epithelial ovarian cancers. Differentiating benign and malignant ovarian masses prior to surgical excision and histopathological evaluation can be challenging given the lack of currently available diagnostic tools and the difficulty in evaluating potential techniques in vivo. The development of animal models for ovarian pathology provides a means of evaluating diagnostic tools and therapeutics as well as a means of understanding pathologic changes in the ovary, specifically the characterization of precursor lesions to malignant transformation.

The incidence of all types of ovarian cancer except germ cell neoplasms increases approximately ten-fold in post-menopausal women,[1] thus the availability of an animal ovarian cancer model mimicking the post-menopausal state would be most applicable to epithelial and stromal ovarian tumors. Recently, a rodent model was developed to mirror the post-menopausal state, utilizing 4-vinylcyclohexene diepoxide (VCD) to accelerate atresia of ovarian follicles. VCD selectively eradicates primordial and primary follicles from the ovary without direct effect on larger, more mature follicles resulting in a gradual onset of ovarian failure with accompanying hormonal changes emulating the human peri-menopausal state.[2-5]

*Correspondence to: Jennifer K. Barton; Email: barton@email.arizona.edu
Submitted: 02/19/10; Revised: 05/27/10; Accepted: 05/31/10
Previously published online: www.landesbioscience.com/journals/cbt/article/12531
DOI: 10.4161/cbt.10.5.12531

Table 1. Animal treatment groups

Group	IP injection (25 d)	Ovarian injection (4 mo post IP injection)	No. rats treated	No. rats included in OCT/LIF analysis
Con/Con	Sesame Oil	Sesame Oil	22	20 (one unilateral LIF)
VCD/Con	VCD	Sesame Oil	18	18
Con/DMBA	Sesame Oil	DMBA	17	17
VCD/DMBA	VCD	DMBA	26	26 (two unilateral LIF)
		Total	83	81

IP, intraperitoneal; mo, months; No., number.

The exposure of the ovary to known carcinogens, such as 7,12-dimethylbenz[a]anthracene (DMBA), is a recently developed approach for inducing ovarian malignancies. The direct application of DMBA to the ovary has been shown to result in selective development of ovarian malignancies in both rats and mice.[2,6-10]

The development of a post-menopausal animal model for ovarian cancer may prove useful in evaluating diagnostic tools to aid in differentiating benign and malignant ovarian pathology and provide better understanding of features characteristic of early cancers to improve their detection. Optical coherence tomography is an emerging, non-destructive imaging modality using near-infrared light to create cross-sectional images of tissue structure with near histological resolution (2–20 μm) with the advantage of up to 2 mm penetration depth compared to other optical technologies which may only have 100 micron or less penetration. OCT has previously been used in a variety of applications, including human eye,[11,12] gastrointestinal neoplasms,[13,14] and gynecologic neoplasms such as ovary,[15-19] endometrium[18-20] and cervix.[18,19,21-26] Prior studies evaluating OCT imaging of human ovarian tissue have shown promising results as a diagnostic tool for ovarian cancer, demonstrating the ability to visualize fine architectural features of both normal ovaries and ovarian malignancies ex vivo[16-18] and in vivo via laparoscopic imaging.[15,19]

Laser-induced fluorescence (LIF) spectroscopy is another non-destructive imaging modality with promising diagnostic capabilities in ovarian cancer. Tissue is illuminated with an ultraviolet to green wavelength of light, exciting fluorophores in tissue such as structural proteins including collagen, and metabolic co-factors nicotinamide adenine dinucleotide (NADH) and flavin adenine dinucleotide (FAD). These fluorophores in turn emit measurable autofluorescence, which provide insight into the biochemical composition of the tissue specimen. Peak emission intensities from collagen, NADH and FAD are typically seen at emission wavelengths of 390, 450 and 550 nm, respectively. LIF has been studied in multiple pathologies,[27] including gynecologic applications such as human cervical neoplasia,[26-31] human ovarian malignancies[16,32] and primate models for ovarian cancer chemopreventative studies.[33,34]

Both OCT and LIF have shown promise in ovarian cancer diagnostics independently. The architectural information provided by OCT is complemented by the biochemical information provided by LIF, thus the combination of these two imaging modalities has potential to characterize ovarian malignancies with higher sensitivity and specificity than either modality alone. In a study of cervical and vulvar cancer, the combination of OCT and LIF resulted in a significant decrease in the number of false positives compared with the false positive rate from each independent modality.[26]

In a previous pilot study, we evaluated the use of combined OCT-LIF in VCD/DMBA treated rats (27 total rats: 34 control ovaries and 20 VCD/DMBA treated ovaries) with DMBA administration issued via a DMBA soaked suture placed within the ovary. OCT and LIF showed promise in characterizing benign and malignant ovaries, however, the treatment protocol resulted in small numbers of atypical (n = 6) and neoplastic (n = 3) ovaries.[35]

In this study, we utilize combined OCT/LIF imaging to optically evaluate the ovaries in large numbers of VCD/DMBA treated and control rats to evaluate normal cyclic, acyclic and neoplastic ovaries, specifically to: (1) determine architectural features visible in OCT to differentiate these tissue categories, (2) further investigate the LIF spectral differences and (3) assess the benefit of combining information obtained with OCT and LIF.

Results

Eighty three rats (166 ovaries) were imaged with combined OCT/LIF. OCT/LIF data from two Con/Con rats was removed from the study due to technical error during imaging. Additionally, the LIF data from one left Con/Con ovary and two left-sided (untreated) VCD/DMBA ovaries was also removed from the analysis due to technical error during LIF imaging (**Table 1**).

Histopathologic evaluation of VCD-treated ovaries demonstrated a lack of functional primary and secondary follicles that were observed in cycling control animals. Although there were some ovulatory follicles present, the majority were degenerating and there was no new follicle development. DMBA treatment was also observed to result in similar features as VCD treatment, however, infrequent primordial and primary follicles were present.

No neoplasms were identified in cycling control Con/Con or Con/DMBA rats. Neoplasm development was identified in four VCD/Con ovaries: (1) one of nine VCD-treated rats at three months (unilateral) and (2) two of nine VCD-treated rats at five months (one rat with unilateral and one rat with bilateral neoplasm development). In rats treated with VCD and subsequent DMBA, a total of thirteen neoplastic ovaries were observed: (1) five of twelve VCD/DMBA animals at three months and (2) eight of fourteen VCD/DMBA animals at five months (all unilateral).

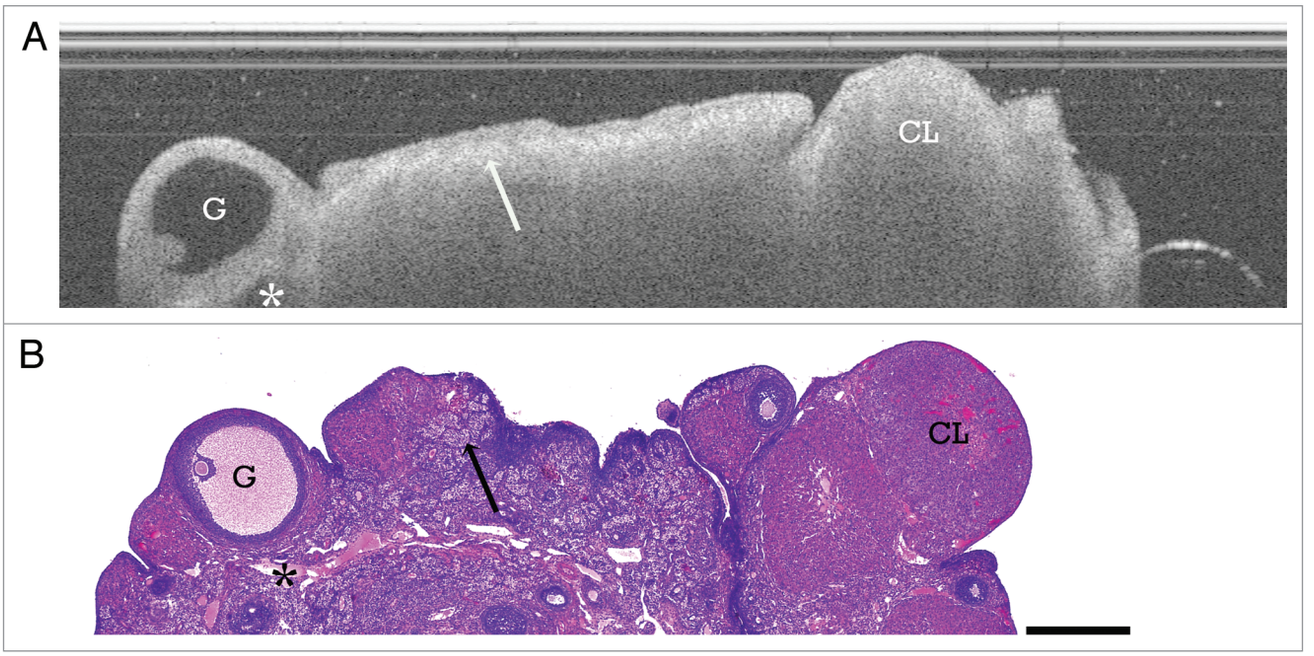

Figure 1. Cyclic ovary. (A) OCT image of cyclic Con/Con ovary and (B) corresponding histology. G, Graafian follicle; CL, corpus luteum; arrow, CL remnants and intervening collagen; asterisk, vascular spaces. OCT image and histology are to scale. Scale bar: 500 μm.

All neoplasms were sex cord-stromal type with Sertoli and Leydig cell components and were confined to the ovary, with the exception of one case which had extension into peri-ovarian fat.

OCT imaging features. Normal cyclic ovaries (Con/Con group: n = 20 rats, 40 ovaries OCT, 39 ovaries LIF) consisted of multiple follicles of varying developmental stage, multiple CL and frequent large regions of CL remnants. Secondary and Graafian follicles were frequently present in OCT imaging of the Con/Con group with well-defined, hyperintense boundaries likely corresponding to stromal collagen surrounding the follicle, an inner layer of homogeneous tissue corresponding to the granulosa cell layer, and a signal-void core representing the antrum (**Fig. 1** and G). Follicular size depended on developmental stage. Frequently, a small, well-defined mass protruding from the follicular wall was visible within the follicle and corresponded to the oocyte and encompassing corona radiata. The zona pellucida could occasionally be visualized as a well-defined, hyperintense band surrounding the oocyte. The size of primary follicles is just within the resolution capabilities of the OCT imaging system and appears to be represented by hyperintense spotting within the ovarian cortex, likely secondary to the stromal collagen surrounding the follicles.

CL are frequently seen in OCT imaging of cycling ovaries and appear as well-circumscribed, homogeneous masses with rapid signal attenuation (**Fig. 1** and CL) likely due to the large amounts of vasculature with red blood cells within the structures being responsible for the signal absorption. Occasional luteal cysts are seen, appearing as a hypointense core within the homogeneous mass (**Fig. 2C** and CL). CL remnants appear as heterogeneous clusters with regions of hypointensity corresponding to the clusters of luteal cells and intervening hyperintense bands (**Fig. 1** and arrow) that mimic the collagen structure intervening through the luteal remnants. CL remnants are frequent and large in the cyclic ovaries and give the stroma a very heterogeneous texture.

Large vascular spaces are seen in stroma of cyclic ovaries, visible as irregularly-shaped hypointense to signal-void regions with well-defined boundaries and occasional underlying shadowing artifacts (**Fig. 1** and asterisk). Although the bursa was removed on most ovaries prior to imaging, small regions of bursal fat are still occasionally seen on the surface of the ovaries and appear as clusters of small, signal-void circles causing shadowing artifact in underlying tissue. Occasionally these structures can be seen within the ovarian stroma and correspond to stromal fat infiltration (**Fig. 2A, B, E and F**).

Acyclic ovaries (including non-neoplastic VCD/Con, Con/DMBA and VCD/DMBA groups: n = 45 rats, 105 ovaries OCT, 103 ovaries LIF) were strikingly different from the cycling ovaries, consisting of increased stromal collagen characterized with OCT by its homogeneous, distinct pattern mimicking the random orientation of stromal collagen (**Fig. 2,** S). Increased numbers of degenerating follicles were aggregated within the ovarian cortex appearing as hyperintense spotting, which resulted in a more heterogeneous texture at the ovarian cortex when present (**Fig. 2** and DF). The acyclic ovaries had significantly decreased numbers of secondary follicles (**Fig. 2**, SF), Graafian follicles, CL and CL remnants (fewer in VCD treated ovaries than in Con/DMBA ovaries). Epithelial invaginations and inclusions were more frequent in the acyclic ovaries (**Fig. 2** and arrows), seen in OCT as well-defined signal-void clefts in the ovarian surface (invaginations) or well-defined circumscribed signal-void regions within ovarian stroma (inclusions). Increased numbers of large

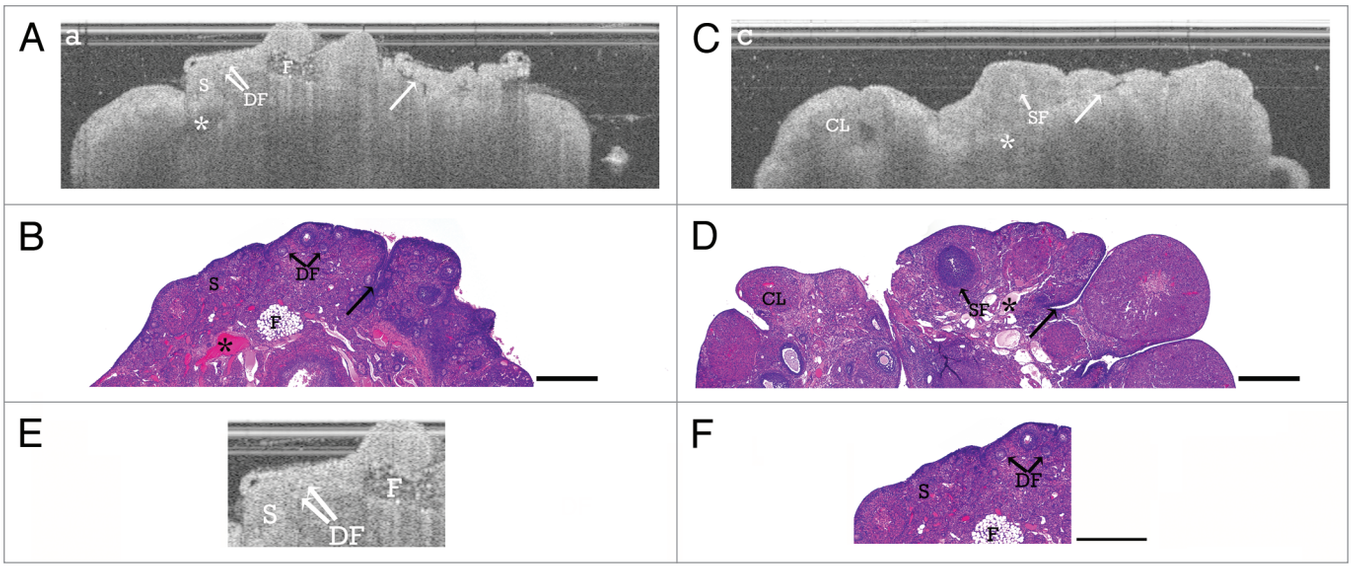

Figure 2. Acyclic ovary. (A) OCT image of acyclic VCD/Con ovary and (B) corresponding histology. (C) OCT image of cyclic Con/DMBA ovary and (D) corresponding histology. (E) Magnification of Figure 2A acyclic VCD/Con ovary and (F) corresponding magnified histology. S, stroma; DF, degenerating follicles; SF, secondary follicle; F, infiltrating fat; CL, corpus luteum with cyst; arrow, epithelial invagination; asterisk, vascular spaces. OCT image and histology are to scale. Scale bar: 500 μm.

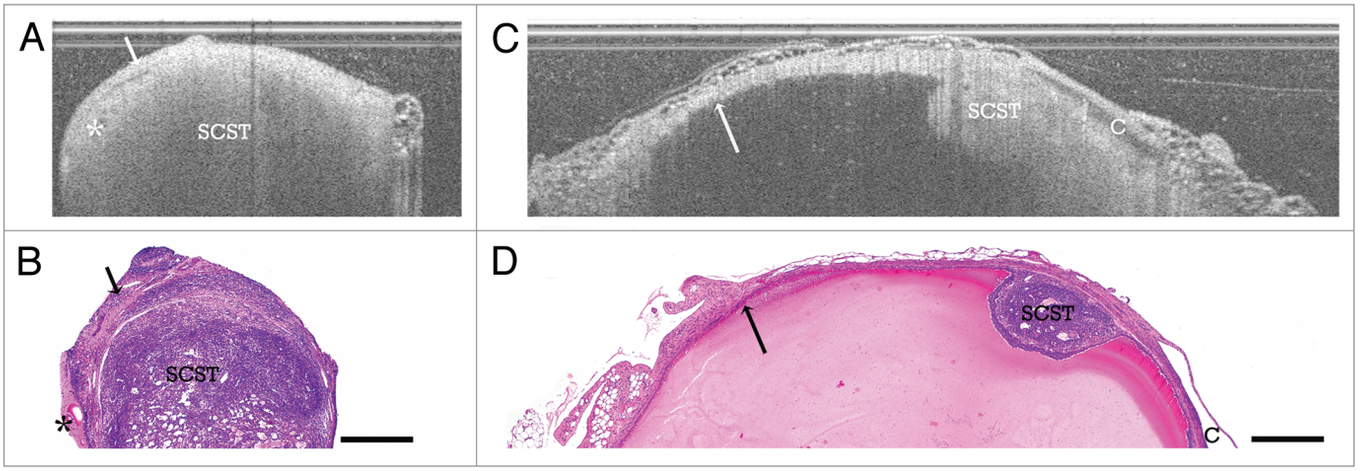

Figure 3. Solid SCST. (A) OCT image of ovary with solid SCST and (B) corresponding histology. SCST, sex cord-stromal tumor; arrow, collagenous capsule; asterisk, vascular spaces**.** (C) OCT image of solid SCST within benign cyst and (D) corresponding histology. SCST, sex cord-stromal tumor; arrow, benign cyst lining; C, adjacent benign cyst. OCT image and histology are to scale. Scale bar: 500 μm.

dilated vascular spaces deep within the stroma in acyclic ovaries are thought to correspond to hypointense irregular spaces with underlying shadowing artifact in OCT (**Fig. 2** and Asterisk).

Sex cord-stromal tumors with predominantly Sertoli-Leydig cell components were identified in 3 VCD/Con treated rats (one bilateral) and 13 VCD/DMBA treated rats (n = 16 rats, 17 ovaries OCT, 17 ovaries LIF) and were classified as either solid (**Fig. 3**), solid with cystic components (**Fig. 4A and B**) or cystic SCST (**Fig. 4C and D**). SCST were characterized with OCT as homogeneous masses with rapid signal attenuation and frequent small hypointense cystic spaces corresponding to malignant tubules (**Fig. 3**, SCST). The SCSTs also display hyperintense borders (**Fig. 3A and B** and arrow) corresponding to the thin collagenous capsules surrounding each neoplastic foci and intervening between foci. The solid tumors frequently had increased dilated vasculature in the surrounding stroma, which is thought to correspond to hypointense irregular spaces with underlying shadowing artifact in OCT (**Fig. 3A and B** and asterisk). In a few cases, solid tumor foci developed within a benign cyst (**Fig. 3C and D**), where a single solid tumor focus, appearing as a homogeneous, rapidly attenuating mass (**Fig. 3C and D**, SCST), protruded into the lumen of a benign cyst, characterized by its clear, well-demarcated lining (**Fig. 3C and D** and Arrow). Occasionally, the solid SCST tumors display a cystic component (**Fig. 4A and B**), which

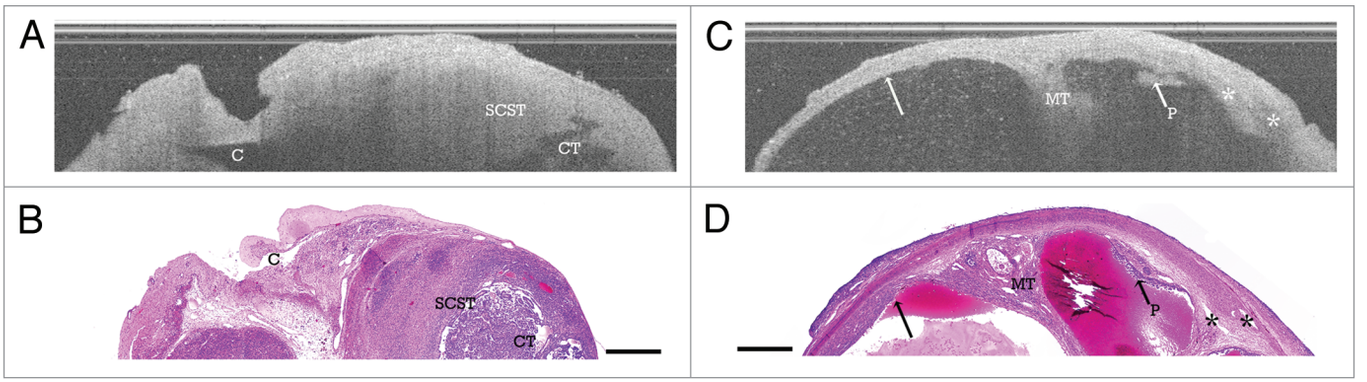

Figure 4. Solid SCST with cystic component and cystic SCST. (A) OCT image of ovary with solid SCST with cystic component and (B) corresponding histology. SCST, Sex cord-stromal tumor; CT, cystic component of SCST; C, adjacent benign cyst (ruptured in histopathology). (C) OCT image of ovary with cystic SCST and (D) corresponding histology. MT, malignant tubules in stroma; P, papillation; arrows, benign cyst lining; asterisk, vascular spaces. OCT image and histology are to scale. Scale bar: 500 μm.

appeared in OCT as small signal-poor to signal-void regions with poorly defined boundaries (**Fig. 4A and B** and CT).

Cystic SCSTs were characterized histologically as multi-cystic masses frequently with simple epithelial lined cysts surrounded by neoplastic tissue. The cyst wall appeared homogeneous in OCT with rapid attenuation, containing visible malignant tubules (**Fig. 4C and D**, MT) and increased vasculature within the surrounding stroma (**Fig. 4C and D** and asterisk). The cysts appeared as signal-void regions with a sharp luminal lining when lined with simple epithelium (**Fig. 4C and D** and arrows). There were also multiple cases where neoplastic tissue encroached on the cyst lining and expanded into the cyst lumen (**Fig. 4C and D**, P) which could be readily visualized on OCT. A summary of these features can be found in **Table 2**.

OCT signal attenuation. Signal attenuation compared between CL and solid SCST revealed a statistically significant ($p = 0.05$) increase in signal attenuation among CL.

LIF spectral comparisons. The LIF spectral curves for all treatment groups are shown in **Figure 5** and a summary of the LIF features for cyclic, acyclic and malignant ovaries can be found in **Table 2**. All groups and tissue types displayed two emission peaks at 390 and 450 nm, corresponding respectively with structural proteins (primarily collagen) and NADH content, and a dip at 420 nm, corresponding to hemoglobin absorption.

We performed comparisons of mean emission spectra at 390, 420 and 450 nm among the five treatment groups to determine if there were differences between benign and malignant ovaries (**Table 3**). There were statistically significant differences between solid and cystic Con/Con and SCST at 390 nm (solid: $p = 0.0026$, cystic: $p = 0.027$), 420 nm (solid: $p = 0.031$, cystic: $p = 0.015$) and 450 nm (solid: $p = 0.012$, cystic: $p < 0.001$) emission. In the comparisons at 390 nm emission, there were statistically significant differences in solid and cystic tissue between Con/DMBA and SCST (solid: $p = 0.0076$, cystic: $p < 0.001$), Con/DMBA and VCD/DMBA (solid: $p = 0.0248$, cystic: $p = 0.049$), Con/Con and VCD/DMBA (solid: $p = 0.0065$, cystic: $p = 0.0126$), and Con/Con and VCD/Con (in the solid tissue comparison only, $p = 0.0242$). Comparisons of 420 nm emission revealed differences between Con/DMBA and SCST (cystic tissue only, $p = 0.048$), ConDMBA and VCD/Con (cystic tissue only, $p = 0.041$), Con/DMBA and VCD/DMBA (solid tissue only, $p = 0.0487$), Con/Con and VCD/Con (solid: $p = 0.0051$, cystic: $p = 0.0115$), and Con/Con and VCD/DMBA (solid tissue only, $p = 0.0011$). Comparisons of solid and cystic tissue at 450 nm revealed differences between Con/DMBA and SCST (solid: $p = 0.0354$, cystic: $p = 0.0017$), VCD/Con and SCST (solid: $p = 0.0422$, cystic: $p = 0.0018$) and Con/Con and VCD/DMBA (solid tissue comparison only, $p = 0.0395$). These results are summarized in **Table 3**.

The ratio of 390 to 450 nm fluorescence emission is compared between solid regions of ConCon (normal cycling) and solid SCST. Using a cut-off of 0.7 AU, 88% sensitivity to SCST and 60% specificity to normal cycling ovaries is achieved (**Fig. 5**).

Discussion

The availability of a reliable model for ovarian neoplasms may provide methods to discriminate between benign and malignant ovaries using non-destructive tools with adequate resolution to resolve fine structural features of ovarian tissue. Optical coherence tomography (OCT) and laser-induced fluorescence (LIF) spectroscopy are complementary imaging modalities, providing high resolution structural imaging and spectral signatures derived from the biochemical composition of tissue specimens, respectively. We utilize combined OCT-LIF to image the ovaries of a post-menopausal rat model of ovarian carcinogenesis. Comparison of OCT images and histopathology demonstrated that OCT could provide information on the microstructural features of cyclic, acyclic and malignant ovary consistent with features described in previous studies of both rat[35] and human ovary.[15-19] LIF was able to characterize spectral differences in fluorescence emission attributed to collagen, NADH/FAD and hemoglobin absorption among cyclic, acyclic and neoplastic ovaries. These findings support the potential application of OCT-LIF to distinguish a benign from a malignant ovary.

Table 2. OCT and LIF imaging features

Category	No.	OCT features	LIF features
Cyclic: Con/Con	40 OCT 39 LIF	**Secondary/Graafian follicles:** Frequent, variably-sized, signal-void core with hyperintense boundary. Often able to visualize oocyte as hyperintense mass within follicle.	**Stroma:** 450 nm peak > 390 nm peak **450 nm peak:** Relatively large amounts of NADH **390 nm peak:** Presence of collagen in stroma **420 nm dip:** Well-defined, corresponds to increased vasculature seen w/i CL **Follicles:** Emission spectra with similar shape to stromal tissue. 420 nm dip poorly-defined, likely due to the absence of hemoglobin
		CL: Frequent, circumscribed homogeneous mass with rapid attenuation. Occ. CL cysts (hypointense core).	
		CL remnants: Numerous hyperintense, heterogeneous clusters mimicking collagen intervening through luteal remnants.	
		Vasculature: Occ. irregularly shaped hypointense/signal-void regions in stroma with well-defined borders.	
Acyclic VCD/Con Con/DMBA VCD/DMBA	105 OCT 103 LIF	**Stroma:** Homogenous, distinct pattern mimics stromal collagen.	**Stroma:** 450 nm peak ≥ 390 nm peak **390 nm peak:** Increasing with treatment group, indicative of high relative collagen content **450 nm peak:** Decreasing with treatment group, due to ovarian quiescence **420 nm dip:** Less pronounced than in cyclic ovaries, likely due to decreased CL numbers **Cysts:** Emission spectra with similar shape to stromal tissue.
		Follicles: Frequent degenerating follicles resulting in heterogeneous texture at ovarian cortex.	
		Epithelial invag/inclusions: Well-defined signal-void clefts (invaginations) or circumscribed signal-void regions (inclusions).	
		CL: Infrequent. More frequent CL cysts.	
		CL remnants: Small, infrequent hyperintense clusters mimicking intervening collagen.	
		Vasculature: Increased dilated vascular spaces deep in stroma, hypointense irregular spaces w/ underlying shadowing.	
Sex cord-stromal tumors: VCD/Con VCD/DMBA	17 OCT 17 LIF	**Solid:** • Rapidly attenuating homogeneous masses • Thin collagenous capsule • Frequent small cystic spaces within solid component corresponding to malignant tubules • Large vascular spaces adjacent to neoplastic masses	**Solid:** 390 nm peak > 450 nm peak. **390 nm peak:** High collagen content from thin collagenous capsule **450 nm peak:** Decreased NADH content c/w slowly proliferating neoplasm **420 nm dip:** Well-defined, increased vasculature associated with tumor development
		Cystic: Multi-cystic masses • Cyst: Signal-void w/ sharp luminal lining • Cyst wall: Neoplastic tissue homogeneous, rapidly attenuating • Few cases of neoplastic foci developing within cyst lining (homogeneous, rapidly attenuating) • Cyst wall papillations visible	**Cystic:** 390 nm peak > 450 nm peak. **390 nm peak:** High collagen content from thin collagenous capsule **450 nm peak:** Less pronounced than solid SCST **420 nm dip:** Less pronounced than solid SCST

No, number ovaries; SCST, sex cord-stromal tumors; CL, corpus luteum; Occ., Occasional; w/, with; w/i, within.

The visualization of precursor lesions and early neoplastic foci is key to improving understanding of ovarian pathogenesis through the development of animal models and new diagnostic tools to differentiate benign ovarian changes from cancer. Specifically, the ability to identify a small solid tumor focus developing within a benign cyst (**Fig. 3C and D**) is promising. In this study and in a prior in vivo study of human ovary,[15] OCT identified epithelial invaginations and inclusions, which are thought to be precursor lesions to aggressive ovarian carcinomas.[37] The high resolution and subsurface imaging capabilities of OCT and LIF allow visualization of these lesions where they would likely be unidentifiable by any method of surface evaluation. OCT and LIF are non-destructive imaging modalities which can be packaged into a small diameter dual modality device.[36,38] As these characteristics provide the means for in vivo imaging, future work should aim to evaluate in vivo ovarian imaging of animal models serially over time to observe tumor progression from early neoplasms or preneoplastic lesions to better characterize these lesions and further enhance understanding of ovarian tumor carcinogenesis.

Laser induced fluorescence spectroscopy was able to successfully elucidate the biochemical compositions of normal cyclic, acyclic and SCST to provide preliminary spectral criteria for differentiating these categories. In comparisons of normal cycling ovaries and SCST, the mean emission intensities were statistically significantly different at 390, 420 and 450 nm in both solid and cystic tissues. As the OCT criteria for solid SCST and CL are quite similar, the ability to distinguish these two entities both with signal attenuation comparisons and fluorescence spectroscopy supports the use of dual modality imaging. In comparisons of 390 nm/450 nm fluorescence emission among solid regions of normal cycling ovaries (containing the largest numbers of CL) and solid SCST, the application of a set cut-off provided a sensitivity of 88% to SCST and a specificity of 60% to normal cycling ovaries. Additionally, the ability to potentially distinguish normal follicles from cystic SCST with fluorescence spectroscopy both complements and strengthens the OCT criteria developed to distinguish these two tissue types.

The LIF spectral findings in this study are consistent with previously reported LIF spectral characterization of human ovarian

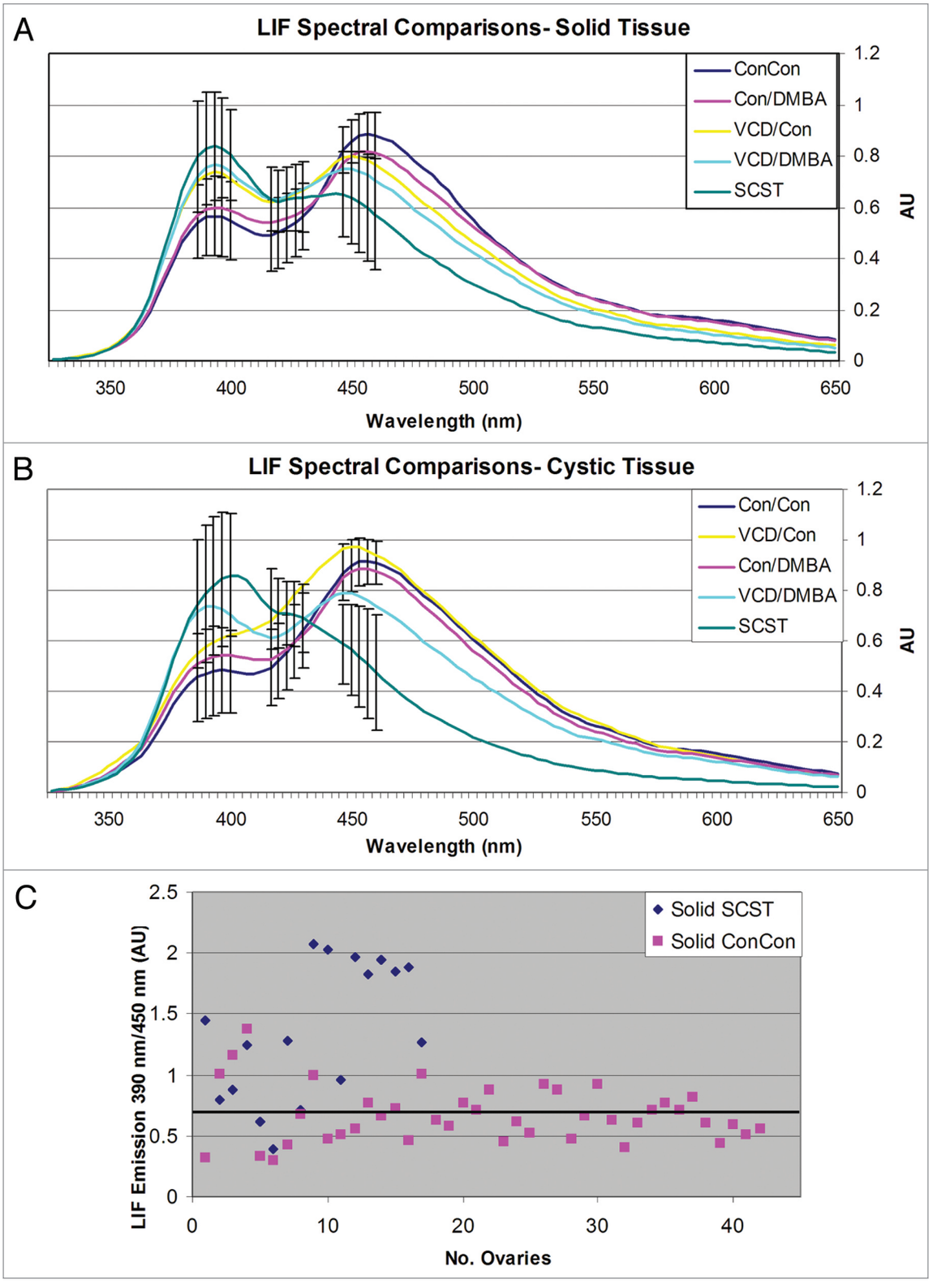

Figure 5. LIF spectral curves. (A) Solid tissue spectral curves. (B) Cystic tissue spectral curves. (C) Scatterplot of the ratio of 390 nm to 450 nm fluorescence emission compared among solid regions of ConCon normal cycling ovaries and solid SCST. Using a cut-off of 0.7 AU (black bar), a sensitivity of 88% to SCST and a specificity of 60% to normal cycling ovaries is achieved. AU: Arbitrary units. No.: Number.

Table 3. LIF spectral comparisons

Tissue at 390 nm em	Solid p-value	Cystic p value
ConCon vs. SCST	0.0026	0.0268
ConDMBA vs. SCST	0.0076	<0.001
ConDMBA vs. VCD DMBA	0.0248	0.049
ConCon vs. ConDMBA	>0.05	>0.05
ConCon vs. VCDCon	0.0242	>0.05
ConCon vs. VCD DMBA	0.0065	0.0126
Tissue at 420 nm em		
ConCon vs. SCST	0.0307	0.015
ConDMBA vs. SCST	>0.05	0.048
ConDMBA vs. VCDCon	>0.05	0.041
ConDMBA vs. VCD DMBA	0.0487	>0.05
ConCon vs. VCDCon	0.0051	0.0115
ConCon vs. VCD DMBA	0.0011	>0.05
Tissue at 450 nm em		
ConCon vs. SCST	0.012	0.0002
ConDMBA vs. SCST	0.0354	0.0017
VCDCon vs. SCST	0.0422	0.0018
VCD DMBA vs. SCST	>0.05	>0.05
ConCon vs. VCD DMBA	0.0395	>0.05

em, emission.

tissue and neoplasms,[16,34] but are inconsistent with the results found in a prior study of fluorescence spectroscopy in a VCD/DMBA treated rat ovarian carcinogenesis model[35] and previous studies of fluorescence spectroscopy in other types of neoplastic tissues, including cervix, colon and bladder,[27] both of which report neoplastic tissues as generally characterized by a relative increase in 450 nm emission due to increased metabolic activity and a relative decrease in 390 nm emission from collagen. Sex cord-stromal tumors have a thin collagenous capsule surrounding the neoplastic mass, which may be the source for the increased 390 nm emission. Second harmonic generation studies of the ovary show an increase in collagen as well as a change in collagen crosslinking which gives an increased signal from collagen and may also be found here.[39] These tumors are characterized as slow growing neoplasms, which may result in decreased metabolic activity and a relative decrease in 450 nm emission from NADH, specifically when compared with metabolically active cycling ovaries.

Differentiating normal follicles, epithelial inclusions and cystic SCST will also be crucial. Given the small size of most epithelial inclusions and the large spot size of the fluorescence excitation beam, we are unable to evaluate if these entities can be distinguished by fluorescence spectroscopy. Future studies will utilize focused-beam fluorescence spectroscopy to evaluate if epithelial inclusions can be distinguished from follicles and cystic neoplasms.

In previous studies of fluorescence spectroscopy in VCD/DMBA treated rat models, DMBA exposure was accomplished by introducing a DMBA soaked suture into the ovary. This resulted in a significant inflammatory reaction which may have resulted in a higher 450 nm emission peak from the metabolic activity of the inflammatory cells. Additionally, the number of tumors in the previous fluorescence spectroscopy study of the VCD/DMBA ovarian carcinogenesis model were small (n = 3) and were a mix of epithelial and stromal tumors, which may also account for the discrepancy in fluorescence signatures.[35] Future studies will be aimed at further characterizing the fluorescence signature of larger numbers of a variety of ovarian neoplasms.

The vast majority of human ovarian malignancies are epithelial in origin.[1] The animal model used in this study expressed stromal ovarian neoplasms, specifically SCST which represent <0.5% of human ovarian malignancies.[40] There is a very large difference between the two forms of ovarian malignancy in stage at time of diagnosis; greater than 75% of epithelial ovarian neoplasms are stage III or IV at the time of diagnosis, but approximately 70% of stromal ovarian neoplasms are at stage I at the time of diagnosis due to more specific symptomology from neoplasm hormone production.[1,40] Although this is a relatively rare cancer, the ability to distinguish an ovarian cancer from benign ovary would have significant clinical utility, particularly if it was confined to the ovary. To date no reliable rodent model of human ovarian cancer exists, so the availability of a rat model capable of providing reliable stromal tumors may be useful in characterizing the pathogenesis of these tumor types. The successful application of OCT-LIF to a rodent model of ovarian cancer providing preliminary imaging criteria to differentiate cyclic ovaries mimicking pre-menopausal human females, acyclic ovaries mimicking post-menopausal human females, and stromal neoplasms is encouraging and should also be applicable to other types of ovarian tumors as it has been evaluated in previous imaging of human epithelial ovarian carcinoma.[2,16] Future studies will evaluate additional animal models with the intent to develop a model for epithelial ovarian cancer. Additionally, as this was a pilot study, the bilateral ovaries of a single animal were included in a given treatment group despite the fact that only the right ovary was treated with saline or DMBA, unless the ovary was found to be neoplastic, in which case it was assigned to the neoplasm group. Histological evaluation and OCT imaging showed no structural differences between the bilateral ovaries of a single rat, indicating that although the treatment was directly applied to the right ovary, the effects of the treatment appear to be systemic. However, in future studies we will treat the bilateral ovaries as dependent but separate in analysis to determine if direct treatment of one ovary has equal effects on the bilateral, untreated ovary.

An additional limitation to this study was the large spot size of the fluorescence incident light (1.25 mm) compared to the OCT lateral resolution (18 μm). Due to this discrepancy, the data are not directly comparable as the fluorescence data encompasses a much larger tissue volume than is depicted in the OCT images. Future studies will be aimed at developing focused OCT-LIF probes such that direct comparisons between OCT and LIF data can be reliably performed.

In this study, we present the successful implementation of combined OCT-LIF to image a post-menopausal rat model of ovarian stromal cancer. Comparison of OCT images and corresponding histopathology allowed for the description of (1)

preliminary microstructural features of normal cyclic ovary including follicles, CL and CL remnants, (2) features of acyclic ovaries including presence of degenerating follicles, increases in stromal collagen, presence of epithelial invaginations/inclusions and vascular changes associated with VCD and DMBA treatment and (3) features of both solid and cystic SCSTs. LIF was able to characterize spectral differences in fluorescence emission attributed to collagen, NADH/FAD and hemoglobin absorption among cyclic ovaries, acyclic ovaries and SCSTs. Additionally, future ex vivo and in vivo imaging will evaluate a finer disease spectrum including normal ovary, benign cyst (simple and inclusion), cyst adenoma, borderline tumors and malignant neoplasms of epithelial origin in addition to neoplasms of stromal and germ cell origin to develop more concrete qualitative and quantitative criteria to aid with differentiation of these entities.

Materials and Methods

Animals. Eighty three female Fisher-344 rats (age d21, Harlan Sprague Dawley) were housed by the University of Arizona Animal Care in microisolators on a 12:12 hr light/dark cycle, constant temperature and humidity, and free access to food and water per NIH guidelines and the policies of the University of Arizona Institutional Animal Care and Use Committee. The animals were allowed a seven day acclimation period before the initiating the experiment. Protocols were approved by the University of Arizona Institutional Animal Care and Use Committee.

VCD treatment. Day 28 old rats received daily (25 d) i.p. injection with either sesame oil vehicle (2.5 ml/kg, Sigma Chemical Company, St. Louis, MO) or VCD (160 mg/kg, Sigma Chemical Company, St. Louis MO).

DMBA treatment. Four months subsequent to the end of VCD dosing, rats (n = 9–14/treatment-timepoint) received a single injection of either sesame oil (vehicle) or DMBA (100 μg DMBA in 10 μl, Sigma Chemical Company, St. Louis MO) under the bursa of the right ovary using a surgical approach.[2] This method was chosen to eliminate the foreign body response possibly caused by an indwelling suture, and preferentially expose the ovarian epithelium to DMBA. Anesthesia was achieved by i.p. injection of 2% Avertin (stock solution: 25 gm tribromoethanol in 15.5 ml 2-butanol; 2 ml stock in 100 ml sterile saline, Aldrich Chemical Company, St. Louis MO). The left ovary was not injected, serving as an internal control.

Animal grouping. Rats were assigned to one of four experimental groups (**Table 1**). Con/Con group (n = 22) received sesame oil by i.p. injection (2.5 ml/kg/day; 25 d) and a single ovarian injection of sesame oil (10 μl) four months after the end of i.p. sesame oil dosing. VCD/Con (n = 18) received VCD (160 mg/kg/day i.p.; 25 d) and a single ovarian injection of sesame oil four months after VCD dosing was completed. Con/DMBA (n = 17) received sesame oil by i.p. injection (25 d) and a single ovarian injection of DMBA (100 μg in 10 μl) four months after the end of sesame oil dosing. VCD/DMBA (n = 26) received VCD (25 d) and a single ovarian injection of DMBA four months after VCD dosing was completed. Ovaries were collected three (n = 8–12/treatment) or five (n = 9–14/treatment) months post-surgery (seven or nine months, respectively, after the end of i.p. VCD or sesame oil dosing).

Optical imaging. Ovaries were harvested at three or five months post DMBA treatment and imaged using a 2-mm diameter side-firing catheter that optically combined both the OCT and LIF subsystems, previously described in detail.[36] The OCT subsystem used a superluminescent diode source with a 1,300 nm center wavelength (D1300-HP, Superlum, Moscow, Russia) with axial and lateral resolutions of approximately 14 μm and 18 μm, respectively. The LIF subsystem used a helium cadmium laser source (Kimmon Electric, Englewood, Colorado) with a 325 nm excitation wavelength, which was chosen due to its ability to excite endogenous fluorophores NADH, FAD and collagen. Excitation light was delivered with a single multimode fiber and fluorescence emission was collected using two separate multimode fibers directed to a spectrometer equipped with a cooled charge-coupled device. The excitation power was 500 μW and integration time was 1 second. The illumination spot size was 1.25 mm. The cut off wavelength of the long pass filter was 50% transmission at 350 nm.

The OCT beam reached focus at 300 microns outside the catheter envelope and the LIF spot size at the corresponding depth was approximately 1 mm. The excitation light power on the tissue was 0.2 mW and the radiant exposure was 0.22 J/cm 2, both within American National Standards Institute maximal permissible exposure levels.

OCT images 6–8 mm lateral by 1.4 mm deep and approximately 5 corresponding LIF spectra/mm in the lateral dimension were acquired simultaneously at 625 μm increments across the dorsal surface of an ovary. A coupling agent (water-based, nonfluorescent lubricant) was used between the catheter and ovary to decrease backreflection from the air-tissue boundary. Data were acquired by a computer and analyzed using Matlab (The Math-Works, Natick, Massachusetts). Time from ovary excision to completion of imaging was less than 30 minutes.

Histology. Ovaries were fixed in Bouin's solution for 2–4 hours, transferred to 70% ethanol, dehydrated, embedded in paraffin blocks and sectioned (5 μm thickness). Every 20th section was mounted and stained with hematoxylin and eosin (H & E).

Optical image analysis. For each animal group (Con/Con, VCD/Con, Con/DMBA and VCD/DMBA), portions of each OCT image and corresponding LIF spectra were classified into one of five histologically confirmed tissue categories: (1) bursal fat, (2) normal cyclic, (3) normal acyclic, (4) benign cyst or (5) neoplastic ovary. OCT images were compared with corresponding histology to identify architectural features associated with each of the above tissue categories. The average maximum fluorescence value was calculated among all spectra. Fluorescence spectra with maximum fluorescence values <10% of the average maximum fluorescence value were removed from analysis due to spectra being low intensity (approximately 3.5% of total fluorescence spectra). LIF spectra were peak normalized and the mean spectra were compared between animal groups/tissue categories. Statistical differences were determined using the Student's t-test. Particular attention was paid to emission peaks at 390 and 450 nm (generally associated with collagen and NADH, respectively) and a dip

at 420 nm (associated with hemoglobin absorption). Because the LIF spectra are highly overlapping and are thus not independent, *N* in the statistical analysis was chosen to be the total number of ovaries in each group from which spectra were compiled.

Signal attenuation comparison analysis. OCT signal attenuation was compared between regions of interest containing histologically confirmed corpora lutea (CL, n = 32 CL in 32 Con/Con ovaries, one corpus luteum per ovary) and solid neoplasms (n = 12 tumors in 12 ovaries, one tumor per ovary). The surface of each structure was manually defined and the image was flattened to the assigned surface. All image columns were averaged and linear fit to the grayscale intensity. Slopes of the intensity decay profiles were averaged over all CL and neoplasms and compared with the one-tailed Student's t-test.

Acknowledgements

These studies were supported by R01s CA119200 (J.K.B) and AG021948 (P.B.H).

References

1. Cancer Facts and Figures. In: American Cancer Society; 2008.
2. Hoyer PB, Davis JR, Bedrnicek JB, Marion SL, Christian PJ, Barton JK, et al. Ovarian neoplasm development by 7,12-dimethylbenz[a]anthracene (DMBA) in a chemically-induced rat model of ovarian failure. Gynecol Oncol 2009; 112:610-5.
3. Kao SW, Sipes IG, Hoyer PB. Early effects of ovotoxicity induced by 4-vinylcyclohexene diepoxide in rats and mice. Reprod Toxicol 1999; 13:67-75.
4. Springer LN, McAsey ME, Flaws JA, Tilly JL, Sipes IG, Hoyer PB. Involvement of apoptosis in 4-vinylcyclohexene diepoxide-induced ovotoxicity in rats. Toxicol Appl Pharmacol 1996; 139:394-401.
5. Hu X, Flaws JA, Sipes IG, Hoyer PB. Activation of mitogen-activated protein kinases and AP-1 transcription factor in ovotoxicity induced by 4-vinylcyclohexene diepoxide in rats. Biol Reprod 2002; 67:718-24.
6. Stewart SL, Querec TD, Ochman AR, Gruver BN, Bao R, Babb JS, et al. Characterization of a carcinogenesis rat model of ovarian preneoplasia and neoplasia. Cancer Res 2004; 64:8177-83.
7. Ting AY, Kimler BF, Fabian CJ, Petroff BK. Characterization of a preclinical model of simultaneous breast and ovarian cancer progression. Carcinogenesis 2007; 28:130-5.
8. Nishida T, Sugiyama T, Kataoka A, Ushijima K, Yakushiji M. Histologic characterization of rat ovarian carcinoma induced by intraovarian insertion of a 7,12-dimethylbenz[a]anthracene-coated suture: common epithelial tumors of the ovary in rats? Cancer 1998; 83:965-70.
9. Crist KA, Zhang Z, You M, Gunning WT, Conran PB, Steele VE, et al. Characterization of rat ovarian adenocarcinomas developed in response to direct instillation of 7,12-dimethylbenz[a]anthracene (DMBA) coated suture. Carcinogenesis 2005; 26:951-7.
10. Tanaka T, Kohno H, Suzuki R, Sugie S. Lack of modifying effects of an estrogenic compound atrazine on 7,12-dimethylbenz(a)anthracene-induced ovarian carcinogenesis in rats. Cancer Lett 2004; 210:129-37.
11. Drexler W. Cellular and functional optical coherence tomography of the human retina: the Cogan lecture. Invest Ophthalmol Vis Sci 2007; 48:5339-51.
12. Chen TC, Zeng A, Sun W, Mujat M, de Boer JF. Spectral domain optical coherence tomography and glaucoma. Int Ophthalmol Clin 2008; 48:29-45.
13. Testoni PA, Mangiavillano B. Optical coherence tomography in detection of dysplasia and cancer of the gastrointestinal tract and bilio-pancreatic ductal system. World J Gastroenterol 2008; 14:6444-52.
14. Suter MJ, Vakoc BJ, Yachimski PS, Shishkov M, Lauwers GY, Mino-Kenudson M, et al. Comprehensive microscopy of the esophagus in human patients with optical frequency domain imaging. Gastrointest Endosc 2008; 68:745-53.
15. Hariri LP, Bonnema GT, Schmidt K, Winkler AM, Korde V, Hatch KD, et al. Laparoscopic optical coherence tomography imaging of human ovarian cancer. Gynecol Oncol 2009; 114:188-94.
16. Brewer MA, Utzinger U, Barton JK, Hoying JB, Kirkpatrick ND, Brands WR, et al. Imaging of the ovary. Technol Cancer Res Treat 2004; 3:617-27.
17. Boppart SA, Bouma BE, Pitris C, Tearney GJ, Fujimoto JG, Brezinski ME. Forward-imaging instruments for optical coherence tomography. Opt Lett 1997; 22:1618-20.
18. Boppart SA, Goodman A, Libus J, Pitris C, Jesser CA, Brezinski ME, et al. High resolution imaging of endometriosis and ovarian carcinoma with optical coherence tomography: feasibility for laparoscopic-based imaging. Br J Obstet Gynaecol 1999; 106:1071-7.
19. Feldchtein F, Gelikonov G, Gelikonov V, Kuranov R, Sergeev A, Gladkova N, et al. Endoscopic applications of optical coherence tomography. Opt Express 1998; 3:257-70.
20. Sergeev A, Gelikonov V, Gelikonov G, Feldchtein F, Kuranov R, Gladkova N, et al. In vivo endoscopic OCT imaging of precancer and cancer states of human mucosa. Opt Express 1997; 1:432-40.
21. Escobar PF, Rojas-Espaillat L, Tisci S, Enerson C, Brainard J, Smith J, et al. Optical coherence tomography as a diagnostic aid to visual inspection and colposcopy for preinvasive and invasive cancer of the uterine cervix. Int J Gynecol Cancer 2006; 16:1815-22.
22. Zuluaga AF, Follen M, Boiko I, Malpica A, Richards-Kortum R. Optical coherence tomography: a pilot study of a new imaging technique for noninvasive examination of cervical tissue. Am J Obstet Gynecol 2005; 193:83-8.
23. Escobar PF, Belinson JL, White A, Shakhova NM, Feldchtein FI, Kareta MV, et al. Diagnostic efficacy of optical coherence tomography in the management of preinvasive and invasive cancer of uterine cervix and vulva. Int J Gynecol Cancer 2004; 14:470-4.
24. Gossage KW, Tkaczyk TS, Rodriguez JJ, Barton JK. Texture analysis of optical coherence tomography images: feasibility for tissue classification. J Biomed Opt 2003; 8:570-5.
25. Pitris C, Goodman A, Boppart SA, Libus JJ, Fujimoto JG, Brezinski ME. High-resolution imaging of gynecologic neoplasms using optical coherence tomography. Obstet Gynecol 1999; 93:135-9.
26. Kuranov RV, Sapozhnikova VV, Shakhova NM, Gelikonov VM, Zagainova EV, Petrova SA. Combined applications of optical methods to increase the information content of optical coherent tomography in diagnostic of neoplastic processes. Quantum Electron 2002; 32:993-8.
27. Ramanujam N. Fluorescence spectroscopy of neoplastic and non-neoplastic tissues. Neoplasia 2000; 2:89-117.
28. Thekkek N, Richards-Kortum R. Optical imaging for cervical cancer detection: solutions for a continuing global problem. Nat Rev Cancer 2008; 8:725-31.
29. Cardenas-Turanzas M, Freeberg JA, Benedet JL, Benedet JL, Atkinson EN, Cox DD, et al. The clinical effectiveness of optical spectroscopy for the in vivo diagnosis of cervical intraepithelial neoplasia: where are we? Gynecol Oncol 2007; 107:138-46.
30. Freeberg JA, Benedet JL, West LA, Atkinson EN, MacAulay C, Follen M. The clinical effectiveness of fluorescence and reflectance spectroscopy for the in vivo diagnosis of cervical neoplasia: an analysis by phase of trial design. Gynecol Oncol 2007; 107:270-80.
31. Drezek RA, Richards-Kortum R, Brewer MA, Feld MS, Pitris C, Ferenczy A, et al. Optical imaging of the cervix. Cancer 2003; 98:2015-27.
32. Brewer M, Utzinger U, Silva E, et al. Fluorescence spectroscopy for in vivo characterization of ovarian tissue. Lasers Surg Med 2001; 29:128-35.
33. Brewer M, Utzinger U, Li Y, Gershenson D, Bast RC Jr, Follen M, et al. Fluorescence spectroscopy as a biomarker in a cell culture and in a nonhuman primate model for ovarian cancer chemopreventive agents. J Biomed Opt 2002; 7:20-6.
34. Brewer M, Utzinger U, Satterfield W, Hill L, Gershenson D, Bast R, et al. Biomarker modulation in a nonhuman rhesus primate model for ovarian cancer chemoprevention. Cancer Epidemiol Biomarkers Prev 2001; 10:889-93.
35. Kanter EM, Walker RM, Marion SL, Brewer M, Hoyer PB, Barton JK. Dual modality imaging of a novel rat model of ovarian carcinogenesis. J Biomed Opt 2006; 11:041123.
36. Tumlinson AR, Hariri LP, Utzinger U, Barton JK. Miniature endoscope for simultaneous optical coherence tomography and laser-induced fluorescence measurement. Appl Opt 2004; 43:113-21.
37. Kurman RJ, Shih Ie M. Pathogenesis of ovarian cancer: lessons from morphology and molecular biology and their clinical implications. Int J Gynecol Pathol 2008; 27:151-60.
38. Hariri LP, Tumlinson AR, Besselsen DG, Utzinger U, Gerner EW, Barton JK. Endoscopic optical coherence tomography and laser-induced fluorescence spectroscopy in a murine colon cancer model. Lasers Surg Med 2006; 38:305-13.
39. Nadiarnykh O, LaComb RB, Brewer MA, Campagnola PJ. Alterations of the extracellular matrix in ovarian cancer studied by second harmonic generation imaging microscopy. BMC Cancer 2010; In press.
40. Young RH, Scully RE. Sex cord-stromal, steroid cell and other ovarian tumors. In: Kurman R, editor. Blaustein's pathology of the female genital tract. 5th ed. New York: Springer-Verlag 2002; 905-66.